Received: 22 April 2022 | Revised: 4 July 2022 | Accepted: 15 July 2022

DOI: 10.1002/er.8464

RESEARCH ARTICLE

INTERNATIONAL JOURNAL OF ENERGY RESEARCH WILEY

Hierarchical carbon nanofibers@tin sulfide nanotube with sulfur-doped carbon layer for ultrafast lithium-storage capability

Ki-Wook Sung | **Hyo-Jin Ahn**

Department of Materials Science and Engineering, Seoul National University of Science and Technology, Seoul, South Korea

Correspondence
Hyo-Jin Ahn, Department of Materials Science and Engineering, Seoul National University of Science and Technology, Seoul 01811, South Korea.
Email: hjahn@seoultech.ac.kr

Funding information
National Research Foundation of Korea, Grant/Award Number: 2019R1 A2 C1005836

Summary

Combining a high-capacity material possessing a core@shell structure with a carbon material is a powerful tactic for reinforcing the performance of Li-ion battery (LIB) anodes. As an efficient and simple approach to obtain tin(II) sulfide (SnS) with ultrafast lithium-storage capability and cycling stability, we propose the hierarchical core@shell structure of carbon nanofibers@SnS nanotubes (CNF@SnSNTs) covered with S-doped carbon via a one-pot carbonization by harnessing the Kirkendall effect of camphene and sulfurization of SnO_2 by L-cysteine. This hierarchical core@shell structure contains mesoporous carbon nanofibers (CNFs) that reduce the Li-ion diffusion pathway, SnS nanotubes (NTs) that expand the active site, and a S-doped carbon layer at the faces of the SnS NTs that promotes the electrical conductivity and inhibits volume expansion of SnS. Therefore, a CNF@SnSNT-C7 electrode achieves superb ultrafast electrochemical performance (528.1 mAh/g under a current density of 2000 mA/g), high specific capacity (2218.2 mAh/g under a current density of 100 mA/g), and an ultrafast cycling stability of 92.9% after 500 cycles under a current density of 2000 mA/g. These performance improvements are resulted from the synergistical effect of mesoporous CNFs, SnS NTs, and S-doped carbon layer. Therefore, CNF@SnSNT is potential anode material for LIBs having superior Li-storage capability.

KEYWORDS

anode materials, hierarchical core@shell structure, lithium-ion batteries, S-doped carbon layer, tin(II) sulfide

1 | INTRODUCTION

With the expanding world energy market, lithium-ion batteries (LIBs) have accepted tremendous concerns owing to their benefits such as large energy density, wide voltage window, high cycling stability, eco-friendliness, and low self-discharge rate. Hence, LIBs have been actively applied as the power source of diverse electrical machine, including smart phones, tablets, and electric vehicles (EVs).[1-4] Owing to the explosive growth of the EV market, LIBs as a central power source require high energy density of 300 Wh/kg, short charging time of 6 minutes, and minimum of 300 miles per charge.[5,6] Therefore, early research on LIBs focused on increasing the specific capacity and cycling stability but is now focused on achieving ultrafast charging capability. Although the Li-ion storage kinetics in anode materials play a major role in realizing ultrafast cycling

performance, graphite, which is the briskly applied anode material in LIBs, has poor lithium-storage kinetics, leading to its poor ultrafast cycling capability. Furthermore, by the poor theoretical capacity of graphite (372 mAh/g), developing alternative anode materials is important to realize high-performance, ultrafast LIBs.[7-9]

Various anode materials that have high theoretical capacities and Li-ion transfer rates have been proposed in view of this goal. Among them, tin(II) sulfide (SnS), which possesses the two-dimensional (2D) layered structure, is a competitive anode material because of its large theoretical capacity (1137 mAh/g) and relatively high Coulombic efficiency.[10] Furthermore, SnS has a lattice interlayer spacing of 4.33 Å, which is advantageous for ultrafast cycling capability because it improves the Li-ion transfer rate.[11] Despite this advantage, its inherently poor electrical conductivity and huge expansion of SnS during cycling results in inferior ultrafast cycling performance with cycling stability of anode.[11] To resolve these difficulties, various approaches to enhance its electrical conductivity and prevent volume expansion have been investigated, resulting in improved anode materials for ultrafast LIBs. For example, one effective strategy is the nanosizing of SnS materials,[12-14] which increases the number of active sites by expanding the specific surface area and boosts the ion-transfer kinetics by diminishing the Li-ion diffusion pathway. Furthermore, the unique nanostructures of nanoflowers, nanobelts, and nanosheets provide an efficient Li-ion transport pathway, facilitating the ultrafast capability of the anode. However, SnS-based nanomaterials tend to degrade easily and aggregate during long-term cycling tests owing to their large volume expansion. To resolve the aforementioned problems as well as the inherently low electrical conductivity, complexation of SnS with carbon materials (such as graphene and carbon nanospheres) has been carried out.[15-17] In these structures, carbon can enhance the inherently poor electrical conductivity of SnS and prevent the volume expansion and agglutination of SnS particles, enhancing the lithium-storage kinetics and cycling stability of the anode. However, the high cost and composite fabrication are serious drawbacks, and uncomplicated efficient process is need if ultrafast LIBs are to be realized using SnS-based nanomaterials as anodes.

Therefore, to satisfy the electrical conductivity, lithium-storage kinetics, and cycling stability of SnS-based anode materials, we propose a unique hierarchical core@shell structure of carbon nanofibers@SnS nanotubes (CNF@SnSNTs) covered with S-doped carbon layers. This was achieved by harnessing the Kirkendall effect of camphene and sulfurization by L-cysteine using a simple one-pot carbonization process. Owing to these synergistical effect of camphene and L-cysteine, S-doped carbon layers covered the surfaces of the SnS NTs. The SnS NT structure increases the number of active sites and mitigates the Li-ion diffusion pathway. Moreover, S-doped carbon layers on face of the SnS prevent volume expansion and increase the electrical conductivity of SnS. With these features, the hierarchical core@shell structure of CNF@SnSNTs covered with S-doped carbon layers can realize excellent specific capacity with cycling stability at ultrafast cycling, making it a superb anode material for LIBs.

2 | EXPERIMENTAL

A hierarchical core@shell structure of CNF@SnSNTs covered with S-doped carbon layers was fabricated using electrospinning and one-pot carbonization. First, 12.5 wt % polyvinylpyrrolidone (PVP; Aldrich), 12.5 wt% tin(II) chloride dihydrate ($SnCl_2{\cdot}2H_2O$; Aldrich), 125 wt% camphene ($C_{10}H_{16}$; Aldrich), and 2.5 vol% acetic acid (CH_3CO_2H; Aldrich) were dispersed in *N*,*N*-dimethylformamide (DMF, C_3H_7NO; Aldrich) at 50°C for 1 hours. For electrospinning, the applied voltage, distance between the collector and needle, and feed rate were retained at 17 kV, 20 cm, and 0.02 mL/h, respectively. The as-spun $SnCl_2$/camphene nanofibers (NFs) were then mixed with L-cysteine ($C_3H_7NO_2S$), heated at 350°C for 10 minutes in air, and carbonized at 500°C for 2 hours in N_2 at a heating rate of 15°C/min. To confirm the L-cysteine effect, we regulated a mass ratio of L-cysteine to the as-spun $SnCl_2$ NFs as 0:1, 1:1, 3:1, 5:1, 7:1, and 10:1. Therefore, the hierarchical core@shell structures of CNF@SnSNTs covered with S-doped carbon layers were successfully fabricated owing to the Kirkendall effect of camphene and sulfurization of SnO_2 by L-cysteine (hereafter referred to as CNF@SnSNT-C0, CNF@SnSNT-C1, CNF@SnSNT-C3, CNF@SnSNT-C5, CNF@SnSNT-C7, and CNF@SnSNT-C10). To prove the camphene effect, we fabricated $SnCl_2$ NFs without camphene, stabilized $SnCl_2$ NFs without camphene, stabilized $SnCl_2$ NFs with camphene, stabilized $SnCl_2$/NFs mixed with L-cysteine, stabilized $SnCl_2$/camphene NFs mixed with L-cysteine (hereafter referred to as as-spun $SnCl_2$ NFs, stabilized $SnCl_2$ NFs, stabilized $SnCl_2$/camphene NFs, and stabilized $SnCl_2$ NFs + cysteine, stabilized $SnCl_2$/camphene NFs + cysteine, respectively), and bare CNF without any additives other than PVP and DMF. In these stabilized samples, the weight ratio of the as-spun NFs to L-cysteine was fixed at 1:7.

To analyze the fabrication mechanism of the CNF@SnSNTs samples, we conducted thermogravimetric

analysis (TGA) of the as-spun $SnCl_2$ NFs and as-spun $SnCl_2$/camphene NFs under a heating speed of 15°C/min. The stabilized $SnCl_2$ NFs, stabilized $SnCl_2$/camphene NFs, stabilized $SnCl_2$ NFs + cysteine, and stabilized $SnCl_2$/camphene NFs + cysteine were also analyzed using field-emission scanning electron microscopy (FESEM) and X-ray diffraction (XRD). The structures of the bare CNFs, CNF@SnSNT-C5, CNF@SnSNT-C7, and CNF@SnSNT-C10 were characterized using FESEM, and the nanostructures with the elemental distribution of CNF@SnSNT-C7 were observed using transmission electron microscopy (TEM) with energy-dispersive spectrometry (EDS) mapping. The porous structures of the fabricated samples were confirmed using N_2 adsorption/desorption isotherm. The component ratios of the fabricated samples were investigated using TGA. X-ray photoelectron spectroscopy (XPS; ESCALAB, with Al K_α X-ray source) was conducted to verify the chemical bonding states of all fabricated samples.

To examine the electrochemical performance of the bare CNFs, CNF@SnSNT-C5, CNF@SnSNT-C7, and CNF@SnSNT-C10, coin cells (CR2032) were produced using the anode of the fabricated samples, a counter electrode of the lithium foil (Honjo Chemical), electrolytic solution of 1.0 M $LiPF_6$ dissolved in a mixed solvent of ethylene carbonate and dimethyl carbonate in a volume ratio of 1:1, and the separator of porous polypropylene membrane (Celgard 2400). To produce the anode, slurries consisting of the fabricated samples as an active material (70 wt%), polyvinylidene fluoride as a binder (20 wt%), and Ketjen black as a conducting carbon (10 wt%) were prepared, coated on the Cu foil, and then dried at 130°C for 12 hours in a vacuum oven. The loading amount of the active materials on all electrodes was 1 ± 0.05 mg/cm^2, and all cells were assembled in an argon-filled glovebox (<5 ppm O_2 and H_2O).

The electrochemical kinetics of all the electrodes were examined using electrochemical impedance spectroscopy (EIS) in the frequency range of 10^5 to 10^{-2} Hz at AC voltage of 5 mV. The galvanostatic charge/discharge test of all the electrodes was conducted using a battery cycler (WMPG 3000S) in the potential range of 0.05 to 3.00 V (vs Li/Li$^+$). The cycling stability was examined for 100 cycles at 100 mA/g, and the rate performances were investigated at current densities of 100, 300, 700, 1000, 1500, and 20 mA/g. Additionally, the ultrafast cycling performance was monitored for 500 cycles under 2000 mA/g. Furthermore, cyclic voltammetry measurements of the bare CNF and CNF@SNSNT-C7 electrodes were conducted using a potentiostat/galvanostat (PGST302N) at in the potential range of 0.05 to 3.00 V (vs Li/Li$^+$) at scan rates of 1 mV/s.

3 | RESULTS AND DISCUSSION

Figure 1 displays schematic images of the formation process of the hierarchical core@shell structure of CNF@SnSNTs covered with a S-doped carbon layer, which was achieved via the Kirkendall effect of camphene and sulfurization of SnO_2 by L-cysteine through one-pot carbonization. During the carbonization process, camphene induces the Kirkendall effect of Sn ions inside the as-spun $SnCl_2$/camphene NFs owing to its low melting point (44°C-48°C).[18] The melted hydrophobic camphene is transformed into hydrophilic isobornyl acetate by acetic acid, which is a polar aprotic solvent. Therefore, Sn ions, PVPs, and isobornyl acetate can coexist in $SnCl_2$/camphene NFs owing to the electrostatic interaction between the Sn ions and their carbonyl oxygen. Consequently, thermally decomposed camphene can increase the rate of the Kirkendall effect owing to its higher diffusion coefficient ($D = \approx 12 \times 10^{-8}$ m^2/s) compared with that of PVP ($D = \approx 3 \times 10^{-8}$ m^2/s). Additionally, SnO_2 particles were formed outside the fibers.[19] Simultaneously, owing to the decomposed camphene with diffused Sn ions, mesopores were formed inside the CNFs. Meanwhile, L-cysteine was thermally decomposed at ≈221°C to produce H_2S, CO_2, and NH_3 gases.[20] Then, the sulfurization reaction of SnO_2 particles located outside the fibers by H_2S gas at 500°C occurred via the following chemical reaction (Equation [1])[21]:

$$SnO_2 + H_2S \rightarrow SnS + H_2O. \quad (1)$$

In Figure S1, while the stabilized $SnCl_2$ NF sample possessed a smooth fiber surface (Figure S1A), the stabilized $SnCl_2$/camphene NF samples contained fibers with SnO_2 particles on the surface (Figure S1B) owing to the Kirkendall effect of camphene. Moreover, the stabilized $SnCl_2$ NF + cysteine sample showed a partial NT structure on the faces of the NFs owing to the sulfurization of SnO_2 in the NFs by L-cysteine (Figure S1C). Furthermore, the stabilized $SnCl_2$/camphene NFs + cysteine sample contained connected SnS NTs owing to the synergistical effect of the Kirkendall effect and sulfurization by camphene and L-cysteine (Figure S1D), that is in good compliance with XRD results (Figure S2). Therefore, the SnS particles formed by the sulfurization of SnO_2 particles were linked to each other, and a final hierarchical core@shell structure of CNF@SnSNTs covered with S-doped carbon layers was obtained. As a result, the SnS NTs can increase the specific capacity owing to the more abundant active sites caused by the extended contact area between SnS and electrolyte both inside and outside the NTs.[22]

FIGURE 1 Schematic images showing the formation mechanism of the hierarchical core@shell structure of the S-doped carbon layer covered CNF@SnSNTs via Kirkendall effect of camphene and sulfurization of SnO_2 by L-cysteine through one-pot carbonization

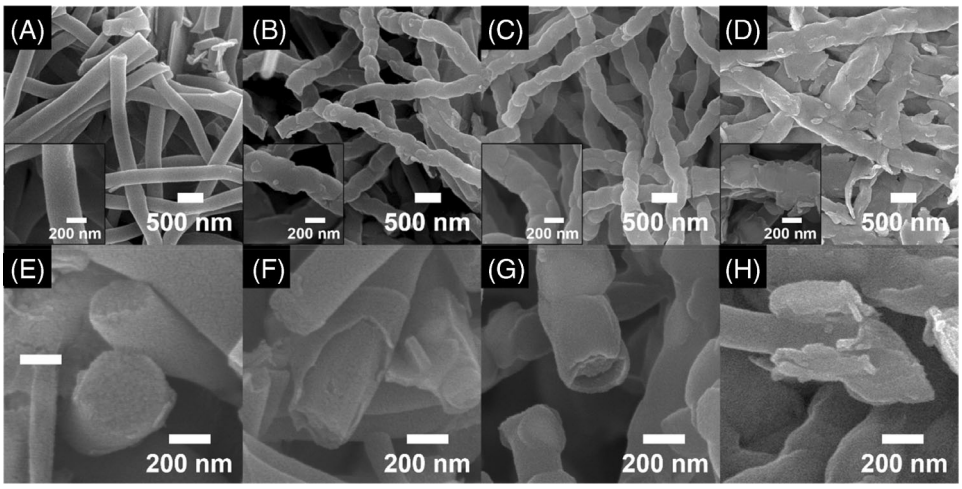

FIGURE 2 (A–D) Low- and (E–H) high-resolution FESEM images of bare CNF, CNF@SnSNT-C5, CNF@SnSNT-C7, and CNF@SnSNT-C10 samples

To determine the optimal amount of L-cysteine, we conducted FESEM analyses of the bare CNF, CNF@SnSNT-C5, CNF@SnSNT-C7, and CNF@SnSNT-C10 samples. As shown in Figure 2A,E, the bare CNF displayed a one-dimensional (1D) fiber structure with a smooth surface, dense cross-sections, and a diameter range of ≈283.9-322.4 nm. In contrast, as shown in Figure 2B,C, the CNF@SnSNT-C5 and CNF@SnSNT-C7 samples contained uniform SnS NTs with a diameter ranges of ≈307.9 to 345.2 nm and 308.2 to 354.8 nm, respectively, and CNFs in the SnS NTs (Figure 2F,G) owing to appropriate sulfurization. However, the CNF@SnSNT-C10 sample contained irregular and agglomerated SnS with diameters ranging from ≈431.6 to

550.3 nm as well as CNFs in the SnS NTs, which is why L-cysteine caused an extreme sulfurization reaction, resulting in the excessive growth of SnS particles. By contrast, the CNF@SnSNT-C0 samples contained CNFs with particle-like SnO_2 NTs owing to the absence of a sulfurization reaction (Figure S3A,B). Additionally, owing to the Kirkendall effect of camphene, the Sn ions migrated outward from the CNFs, forming mesopores inside. In particular, owing to the optimized L-cysteine effect, the CNF@SnSNT-C7 samples had the highest specific surface area and mesoporous fraction (Figure S4 and Table S1). Thus, for the CNF@SnSNT-C7 samples, the mesoporous CNFs in the hierarchical core@shell structure of the CNF@SnSNTs inhibit the Li-ion diffusion pathway, enhancing the ultrafast electrochemical performance.[23,24]

To further analyze the nanostructure, we used TEM to analyze the CNF@SnSNF-C7 sample. In the low-resolution TEM images (Figure 3A), the CNF@SnSNF-C7 sample possessed a 1D nanotube structure with diameters ranging from ≈309.7 to 350.4 nm. Furthermore, in the magnified TEM images (Figure 3B), a comparatively bright contrast is apparent at the middle of the CNF@SnSNF-C7 sample, which represent the internal CNFs, while the dark contrast in the outside area corresponds to the external SnS NTs covered with a carbon layer. Additional bright regions were observed in the CNFs, signifying the mesopores formed by the decomposition of camphene with the diffusion of Sn ions. In the magnified TEM images, as shown in Figure 3C, we noted that the carbon layer, which had a thickness of ≈12.11 to 13.43 nm, was coated on the SnS having a lattice distance of 0.28 nm, corresponding with (111) plane of orthorhombic SnS. These results demonstrate that during one-pot carbonization, orthorhombic SnS was successfully formed by the sulfurization reaction, and carbon layers were formed on the face of the SnS by decomposed PVP. In addition, we conducted EDS mapping to analyze the elemental distribution of the CNF@SnSNT-C7 sample (Figure 3D), which revealed that C was well-dispersed along the CNFs and Sn and S along the NTs, suggesting that the SnS NTs were well-located outside the CNFs. Therefore, we confirmed that the face of SnS was uniformly covered by the carbon layers, and this structure not only increased the cycling stability by preventing the volume expansion of SnS but also enhanced the electrical conductivity of SnS.[22]

To demonstrate the change in the crystal structure owing to the L-cysteine effect, XRD analyses of the bare CNF, CNF@SnSNT-C5, CNF@SnSNT-C7, and CNF@SnSNT-C10 samples were conducted. In Figure 4A, the bare CNF gives rise to broad peaks at ≈26.0°, which correspond with the (002) plane of amorphous graphitic carbon. However, the CNF@SnSNT-C5, CNF@SnSNT-C7, and CNF@SnSNT-C10 samples showed diffraction peaks at approximately 20.0°, 26.0°, 27.4°, 30.4°, 31.5°, 39.0°, and 45.4°, which is a convincing proof of the formation of the orthorhombic SnS phase with (110), (120), (021), (101), (111), (131), and (002) (JCPDS card No. 39-0354), respectively, via the L-cysteine effect. Furthermore, we confirmed that all SnO_2 were transferred to SnS via an efficient sulfurization reaction when the weight ratio of L-cysteine to as-spun $SnCl_2$ fibers was 3 or more (Figure S5). Additionally, the magnified XRD curves in Figure 4B show that two peaks corresponded with the (101) and (111) planes gradually shift toward lower angles from CNF@SnSNT-C5 to

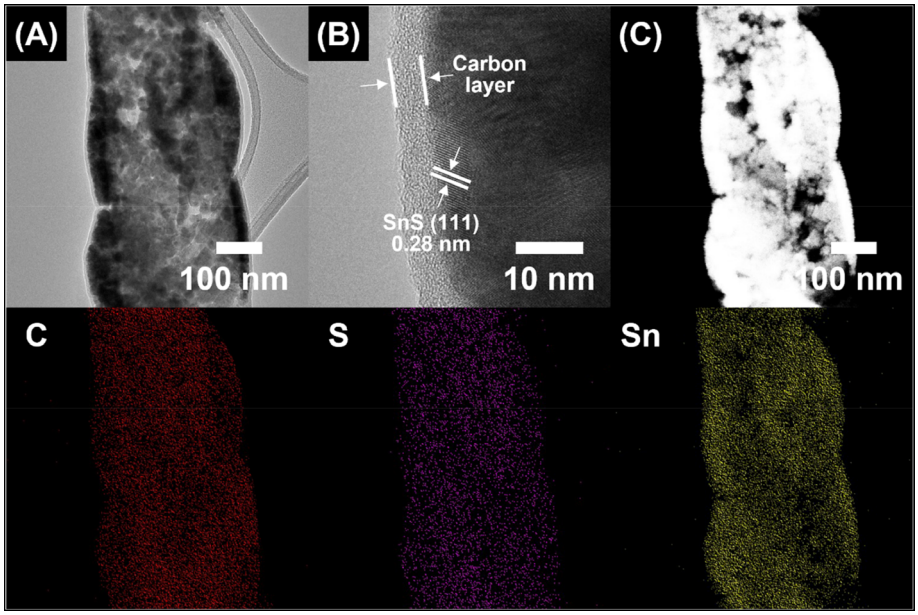

FIGURE 3 (A) Low- and (B,C) high-magnification TEM images of CNF@SnSNT-C7, and (D) EDS mapping results of C, S, and Sn elements

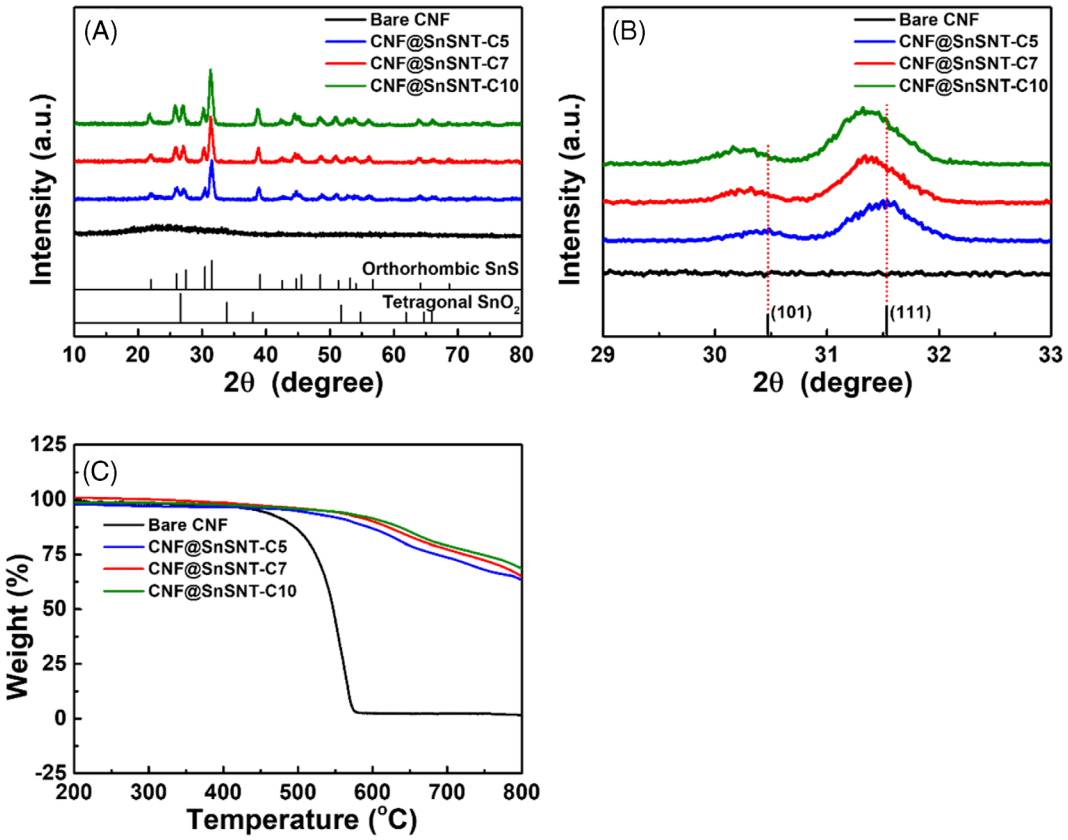

FIGURE 4 (A) XRD patterns, (B) magnified XRD results in the range of 29° to 33°, and (C) TGA curves of bare CNF, CNF@SnSNT-C5, CNF@SnSNT-C7, and CNF@SnSNT-C10 samples

CNF@SnSNT-C10, indicates the extended interlayer distance of SnS owing to the increased insertion of S ions as a result of the increased amount of L-cysteine.[25,26] The extended interlayer distance can also increase the ion-transfer rate; therefore, the ultrafast cycling capability gradually increased from CNF@SnSNT-C5 to CNF@SnSNT-C10.[25,27,28] In Figure 4C, TGA was carried out to confirm the component ratios of all samples. Although the bare CNF exhibited complete weight loss, the fabricated core-shell structures underwent partial weight loss (CNF@SnSNT-C5: 36.84%; and CNF@SnSNT-C10: 31.12%), implying that the inserted S ions in the layered SnS and doped S atoms in the carbon layer increased owing to the enhanced L-cysteine effect. Therefore, the SnS NTs in the hierarchical core@shell structure of CNF@SnSNTs-C7 have a high specific capacity and enhance the ultrafast cycling capability.

To elucidate the chemical bonding state of all samples, we performed XPS analyses of the bare CNF, CNF@SnSNT-C5, CNF@SnSNT-C7 and CNF@SnSNT-C10 samples; all spectra were calibrated by the C 1s binding energy of approximately 284.5 eV. In Figure 5A, the C 1s XPS spectra display four special peaks at ≈284.5, 286.0, 287.6, and 288.9 eV, according with C—C, C—N/C—O/C—S, C═O, and O—C═O bonding states, respectively.[29-31] The peak-area ratios of C–N,O,S to C—C gradually increased from CNF@SnSNT-C5 (0.25) to CNF@SnSNT-C10 (0.36), indicating increased S doping in the carbon layer. In the Sn 3d XPS spectra (Figure 5B), the CNF@SnSNTs samples, excluding the bare CNF, displayed two characteristic peaks at approximately 485.9 and 494.3 eV, that were equivalent in the Sn^{2+} $3d_{5/2}$ and Sn^{2+} $3d_{3/2}$ states, suggesting that no SnO_2 remained owing to the efficiency of sulfurization. These consequences are well matched with the XRD consequences.[32,33] Although the bare CNF exhibits no characteristic peaks at the S 2*p* XPS spectra, in Figure 5C, the CNF@SnSNT samples give rise to four special peaks at ≈160.5, 161.8, 162.9, and 163.7 eV, according with SnS $2p_{3/2}$, SnS $2p_{1/2}$, C—S—C $2p_{3/2,}$ and C—S—C $2p_{1/2}$, respectively.[32,33] The enhanced C—S—C peak intensities indicate that the doped S atoms in the carbon layer increase with increasing amount of L-cysteine, and the doped S atom is located between two C atoms as thiophenic-S, which can increase the electrical conductivity by providing additional electrons by spin-orbit coupling.[32,33]

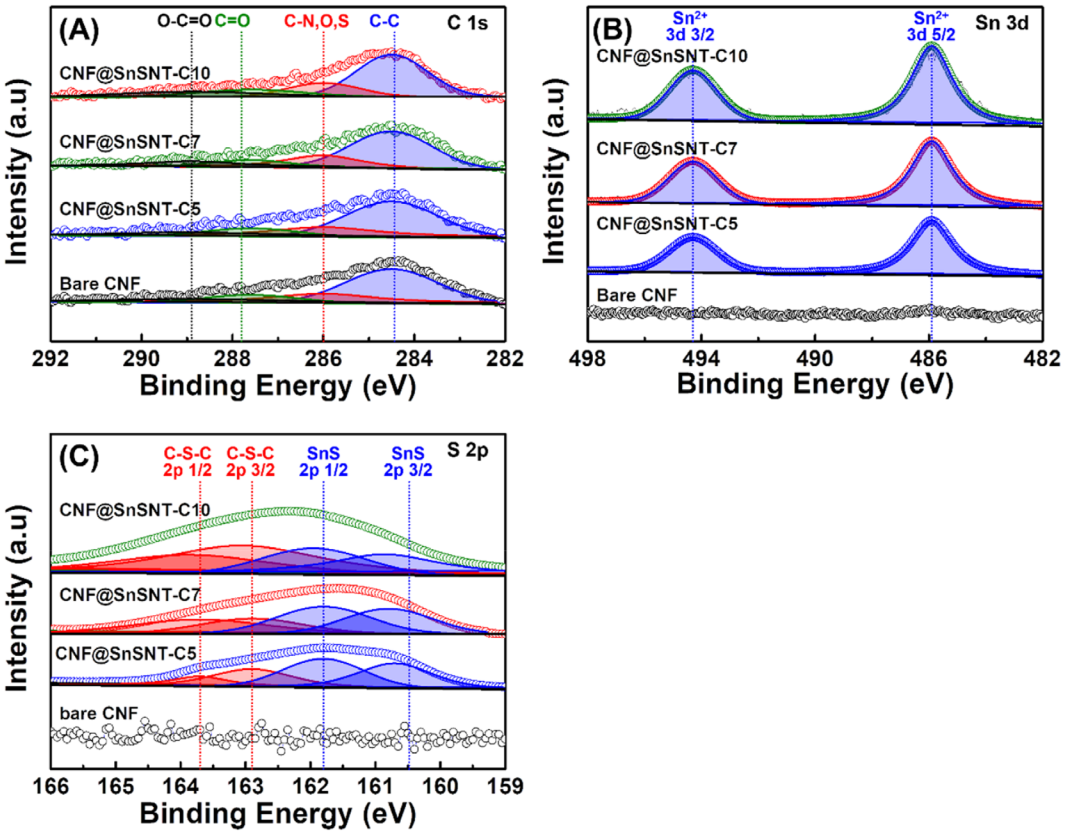

FIGURE 5 XPS spectra of (A) C 1s, (B) Sn 3d, and (C) S 2p of bare CNF, CNF@SnSNT-C5, CNF@SnSNT-C7, and CNF@SnSNT-C10 samples

Therefore, the development of the S-doped carbon layer improved the ultrafast lithium-storage capability by enhancing the electrical conductivity of the S-doped carbon layers on the SnS NTs.

To explore the electrochemical kinetics, we conducted EIS analyses of the bare CNF, CNF@SnSNT-C5, CNF@SnSNT-C7, and CNF@SnSNT-C10 electrodes. In the Nyquist plot, the semicircle at high-frequency area denotes the charge-transfer resistance (R_{ct}), and the tipped line at the low-frequency area indicates the Warburg impedance. The CNF@SnSNT-C7 electrode exhibited the smallest R_{ct} and thus the highest electrical conductivity owing to the S-doped carbon layers on SnS, as shown in Figure 6A. According to the XPS results, the CNF@SnSNT-C10 sample had the highest amount of S doping amount in the carbon layer; this electrode exhibited a high R_{ct} owing to the agglomeration of SnS as a result of excessive sulfurization. Moreover, with respect to the Warburg impedance (Figure 6B), the CNF@SnSNT-C7 electrode displayed the lowest value among all the electrodes. Knowing the Warburg impedances, the Li-ion diffusion coefficients of all the electrodes could then be calculated using Equations (2) and (3)[34,35]:

$$Z_{real} = R_e + R_{ct} + \sigma_w \omega^{-1/2}, \tag{2}$$

$$D = R^2T^2/2A^2n^4F^4C^2\sigma_w, \tag{3}$$

where R_e, σ_w, D, R, A, n, T, F, and C represent the bulk resistance, Warburg impedance, Li-ion diffusion coefficient, gas constant, temperature, electrode area, number of electrons, Faraday's constant, and molar concentration, respectively. Compared with the bare CNF electrode ($D = 6.3 \times 10^{-14}$ cm^2 s^{-1}), the CNF@SNSNT-C5, CNF@SnSNT-C7, and CNF@SnSNT-C10 electrodes had higher Li-ion diffusion coefficients of 16.8×10^{-14}, 19.3×10^{-14}, and 14.7×10^{-14} cm^2 s^{-1}, respectively, due to the mesopores of the CNF structure. However, the CNF@SnSNT-C10 electrode had a lower Li-ion diffusion coefficient owing to the reduced mesopore volume as a consequence of the agglomerated NT structure. Therefore, ultrafast Li-ion storage performance of the CNF@SnSNT-C7 electrode was highest owing to the boosted electrochemical kinetics owing to the optimized L-cysteine effect.

The electrochemical performances of the bare CNF, CNF@SnSNT-C5, CNF@SnSNT-C7, and CNF@SnSNT-C10

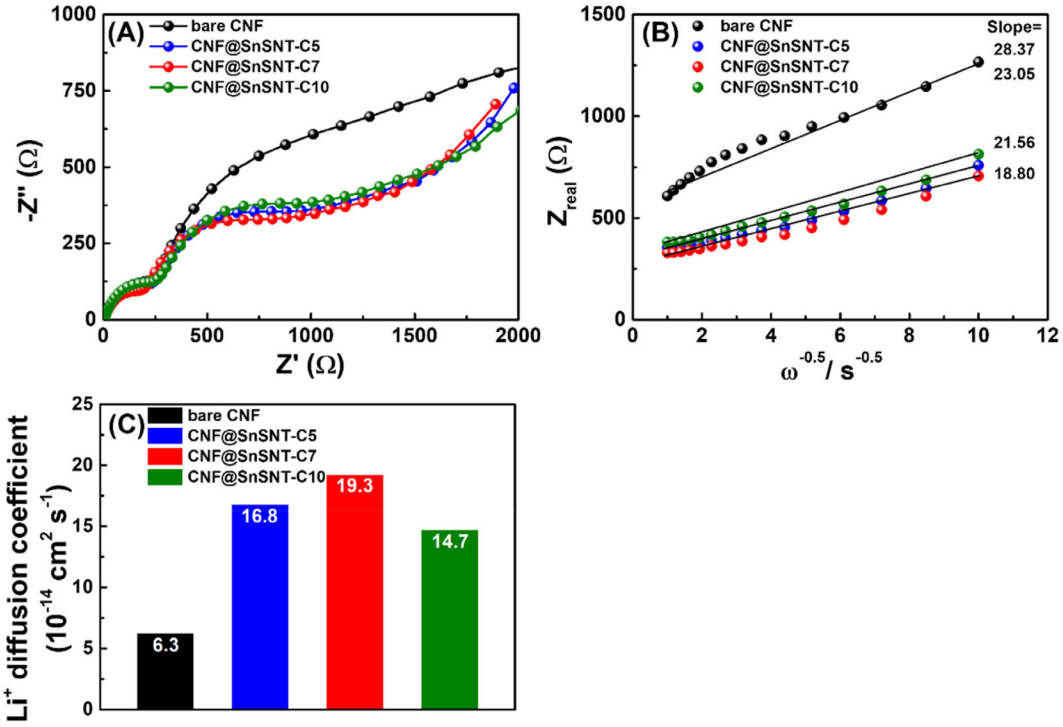

FIGURE 6 (A) Nyquist plots, (B) relationship between Z_{real} and $\omega^{-1/2}$, and (C) Li-ion diffusion coefficients of bare CNF, CNF@SnSNT-C5, CNF@SnSNT-C7, and CNF@SnSNT-C10 electrodes

electrodes were investigated using galvanostatic charge/discharge tests. In the cycling stability test (Figure 7A), compared with the bare CNF electrode, the CNF@SnSNT electrodes exhibited higher initial discharge capacity because of a large theoretical specific capacity of SnS with large number of active sites provided by the hierarchical core@shell structure of CNF@SnSNTs. Furthermore, to clarify the reversible capacity, the charge capacities of all the electrodes are displayed in Figure S6. In particular, the CNF@SnSNT-C7 electrode exhibited a superb initial discharge capacity (2218.2 mAh/g) compared with the other CNF@SnSNT electrodes (1798.8 mAh/g for CNF@SnSNT-C5 and 1627.2 mAh/g for CNF@SnSNT-C10) owing to its optimum NT structure as a result of the L-cysteine effect, as confirmed by the SEM results. The galvanostatic charge/discharge curves distinctly display two voltage plateaus during the first discharging process at ≈1.3 V, coinciding with the transformation of SnS ($SnS + 2Li^+ + 2e^- \rightarrow Li_2S + Sn$), and below 0.76 V, coinciding with alloying reaction of Sn ($Sn + 2Li^+ + 2e^- \rightarrow Li_2Sn$), as shown in Figure S7.[21,26,36] The Coulombic efficiencies of all electrodes got to ≈100% after 8 cycles, indicating the reversible charge/discharge reaction, and the CNF@SnSNT-C7 electrode displayed a high cycling stability (81.0%) and superb discharge capacity (859.8 mAh/g) after 100 cycles compared with the CNF@SnSNT-C5 (74.4% with 674.6 mAh/g) and CNF@SnSNT-C10 (67.1% with 467.2 mAh/g) electrodes. These results indicate that the optimized hierarchical core@shell structure of the CNF@SnSNTs covered with a S-doped carbon layer increases the specific capacity by rising the number of active sites, improving the cycling stability, by preventing the volume expansion of SnS due to carbon layers. Figure 7B displays the rate performances about all electrodes. Based on the rise in current density of 100 to 2000 mA/g, the CNF@SnSNT-C7 electrode demonstrated the best capacity retention of 54.6% compared with the other electrodes (35.2%, 45.3%, and 43.7% for bare CNF, CNF@SnSNT-C5, and CNF@SnSNT-C10, respectively). Additionally, as the current density began to return to 100 mA/g, the CNF@SnSNT-C7 electrode displayed an excellent reversible capacity (91.2%) compared with the CNF@SnSNT-C5 (88.5%) and CNF@SnSNT-C10 (76.4%) electrodes. The superb rate capability of the CNF@SnSNT-C7 electrode is ascribed to its electrical conductivity, which was reinforced by S-doped carbon layers at the faces of SnS and the mesoporous CNFs on account of the diminished Li-ion diffusion path. Furthermore, to examine the influence about hierarchical core@shell structure of in the CNF@SnSNTs covered with S-doped carbon layers on the ultrafast cycling performance, all electrodes were subjected to an ultrafast cycling test under a current density of 2000 mA/g, as shown in Figure 7C. After 500 cycles, compared with the other

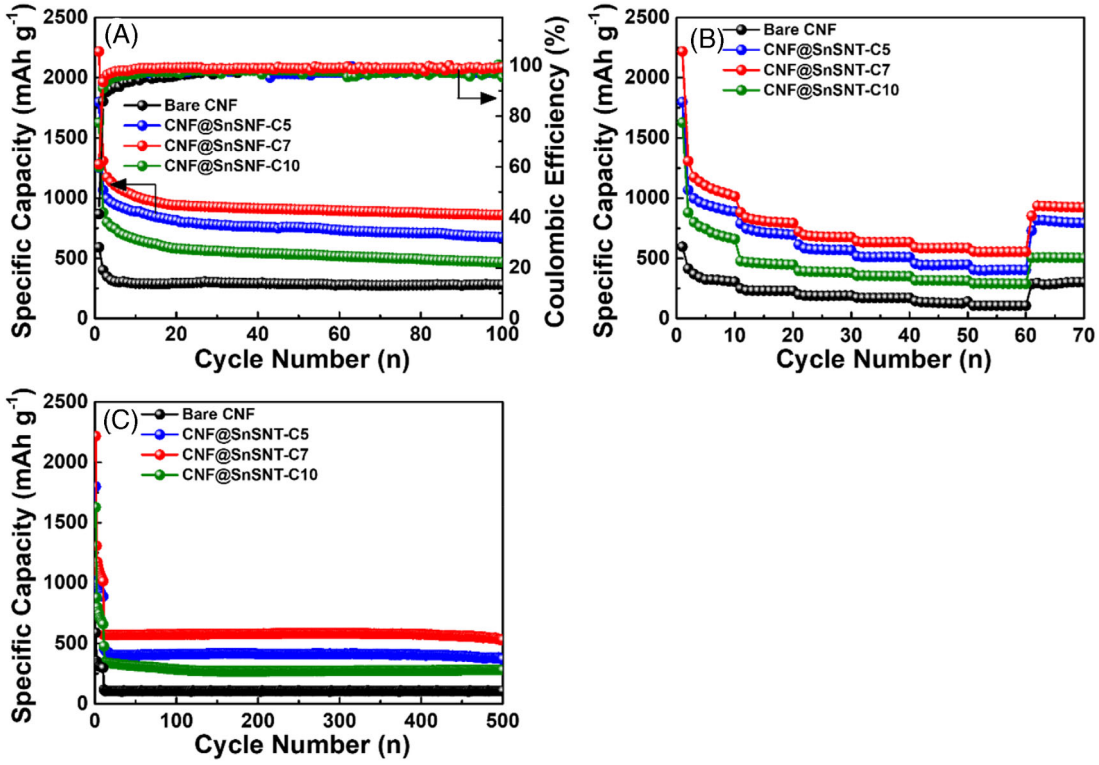

FIGURE 7 (A) Cycling stability, (B) rate performance, and (C) ultrafast cycling performance of bare CNF, CNF@SnSNT-C5, CNF@SnSNT-C7, and CNF@SnSNT-C10 electrodes

electrodes (80.8% with 369.9 mAh/g for CNF@SnSNT-C5, and 79.5% with 278.5 mAh/g for CNF@SnSNT-C10), the CNF@SnSNT-C7 electrode demonstrated superior ultrafast cycling capability along with a cycling stability of 92.9% and specific capacity of 528.1 mAh/g. Furthermore, we conducted cyclic voltammetry measurements of the bare CNF, CNF@SnSNT-C5, CNF@SnSNT-C7, and CNF@SnSNT-C10 electrodes to clarify the electrochemical reactions of CNF@SnSNT-C7. In Figure S8, the CNF@SnSNT electrodes exhibit cathodic peaks at ≈1.2 V, corresponding with the reaction of SnS with Li^+ ions ($SnS + 2Li^+ + 2e^- \rightarrow Li_2S + Sn$), and at ≈0.5 V, corresponding with the multistep alloying process of Sn ($Sn + 2Li^+ + 2e^- \rightarrow Li_2Sn$), which are in accordance with the charge-discharge profile.

This remarkable ultrafast electrochemical performance with stability of the CNF@SnSNT-C7 electrode are explained as follows: (I) the mesoporous CNFs formed by the decomposition of camphene with diffused Sn ions reduced the Li-ion diffusion pathway; (II) the SnS NTs prepared via the Kirkendall effect of camphene and sulfurization of SnO_2 by the L-cysteine effect resulted in excellent specific capacity by rising the number of active sites; and (III) the S-doped carbon layers on the face of the SnS NTs, formed during the carbonization and sulfurization reactions, enhanced the ultrafast cycling stability by preventing the volume expansion of SnS during cycling and increasing electrical conductivity.

4 | CONCLUSIONS

In this study, we prepared hierarchical core@shell structures of S-doped carbon layer covered CNF@SnSNTs via a one-pot carbonization process by harnessing the synergistic effects of camphene with L-cysteine. This causes enhancements in the electrical conductivity, lithium-storage kinetics, and cycling stability of the ultrafast LIBs anode. During carbonization, SnO_2 particles were formed on the faces of the NFs owing to the Kirkendall effect of camphene. Then, SnS NTs were formed owing to sulfurization by L-cysteine. Simultaneously, S-doped carbon layers were developed on the faces of the SnS NTs, and the interlayer distance of SnS increased upon the insertion of S ions. A 1:7 the weight ratio of the as-spun $SnCl_2$ NFs to L-cysteine (CNF@SnSNT-C7) led to excellent coverage of the hierarchical core@shell structure with the S-doped carbon layer, large mesoporous pore volume, and increased interlayer distance of SnS by optimizing the L-cysteine effect. Therefore, the CNF@SnSNT-C7 electrode demonstrated a superior discharge capacity of 859.8 mAh/g and cycling stability of 81.0%. Furthermore, during the ultrafast cycling test (current density of

2000 mA/g), the CNF@SnSNT-C7 electrode demonstrated a superb specific capacity of 528.1 mAh/g with a cycling stability of 92.9%, which is ascribed to the synergistical effect of the hierarchical core@shell structure of the CNF@SnSNTs covered with the S-doped carbon layer. This ultrafast cycling capability resulted from the mitigation of the Li-ion diffusion path by the mesoporous CNFs as well as the ingibition of volume expansion of SnS and increase of electrical conductivity by the S-doped carbon layers on the faces of the SnS NTs, while the high specific capacity was due to the increased number of active sites in the SnS NTs. In conclusion, the novel hierarchical core@shell structure of CNF@SnS, because of its large specific surface area, mesoporosity, and S-doped carbon layer, leads to ultrafast lithium-storage capability with cycling stability, making this a hopeful anode material for ultrafast LIBs.

ACKNOWLEDGEMENT

This work was supported by the National Research Foundation of Korea (NRF) grant funded by the Korea government (MSIT) (No. 2019R1 A2 C1005836).

DATA AVAILABILITY STATEMENT

Data available in article supplementary material.

ORCID

Ki-Wook Sung https://orcid.org/0000-0001-6546-623X
Hyo-Jin Ahn https://orcid.org/0000-0002-5786-3937

REFERENCES

1. Armand M, Tarascon J-M. Building better batteries. *Nature*. 2008;451:652. doi:10.1038/451652a
2. Bruce PG, Scrosati B, Tarascon J-M. Nanomaterials for rechargeable lithium batteries. *Angew Chem Int Ed*. 2008;47:2930. doi:10.1002/anie.200702505
3. Liang C, Gao M, Pan H, et al. Lithium alloys and metal oxides as high-capacity materials for lithium-ion batteries. *J Alloys Compd*. 2013;575:246. doi:10.1016/j.jallcom.2013.04.001
4. An G-H, Lee D-Y, Ahn H-J. Carbon-encapsulated hollow porous vanadium-oxide nanofibers for improved lithium-storage properties. *ACS Appl Mater Interfaces*. 2016;8:19466. doi:10.1021/acsami.6b05307
5. Nayak PK, Yang L, Brehm W, et al. From lithium-ion to sodium-ion batteries: advantages, challenges, and surprises. *Angew Chem Int Ed*. 2018;57:102. doi:10.1002/ange.201703772
6. Shin D-Y, Ahn H-J. Interfacial engineering of a heteroatom-doped graphene layer on patterned aluminum foil for ultrafast lithium-storage kinetics. *ACS Appl Mater Interfaces*. 2020;12:19210. doi:10.1021/acsami.0c01774
7. An G-H, Kim H, Ahn H-J. Excavated carbon with embedded Si nanoparticles for ultrafast lithium-storage. *J Ind Eng Chem*. 2018;68:146. doi:10.1016/j.jiec.2018.07.039
8. Grey CP, Hall DS. Prospects for lithium-ion batteries and beyond—a 2030 vision. *Nat Commun*. 2020;11:6279. doi:10.1038/s41467-020-19991-4
9. Wu X, Xia S, Huang Y, et al. High-performance, low-cost, and dense-structure electrodes with high mass loading for lithium-ion batteries. *Adv Funct Mater*. 2019;29:1903961. doi:10.1002/adfm.201903961
10. Jiang Y, Ding Y, Chen F, et al. Structural phase transformation from SnS_2/reduced graphene oxide to SnS/sulfur-doped graphene and its lithium-storage properties. *Nanoscale*. 2020;12:1697. doi:10.1039/c9nr08075a
11. Cui Z, He S-A, Liu Q, et al. Graphene-like carbon film wrapped tin (II) sulfide nanosheet arrays on porous carbon fibers with enhanced electrochemical kinetics as high-performance Li and Na ion battery anodes. *Adv Sci*. 2017;7:1903045. doi:10.1002/advs.201903045
12. Vaughn DD, Hentz OD, Chen S, et al. Formation of SnS nanoflower for lithium ion batteries. *Chem Commun*. 2012;48:5608-5610. doi:10.1039/c2cc32033a
13. Lu J, Nan C, Li L, et al. Flexible SnS nanobelts: facile synthesis, formation mechanism and application in Li-ion batteries. *Nano Res*. 2016;6(1):55. doi:10.1007/s12274-012-0281-7
14. Kang J-G, Park J-G, Kim D-W. Superior rate capabilities of SnS nanosheet electrodes for Li ion batteries. *Electrochem Commum*. 2012;12:307. doi:10.1016/j.elecom.2009.12.025
15. Deng Z, Jiang H, Hu Y, et al. Nanospace-confined synthesis of coconut-like SnS/C nanospheres for high-rate and stable lithium-ion batteries. *AICHE J*. 2018;64:6. doi:10.1002/aic.16068
16. Wei Z, Wang L, Zhuo M, et al. Layered tin sulfide and selenide anode materials for Li- and Na-ion batteries. *J Mater Chem A*. 2018;6:12185. doi:10.1039/c8ta02695e
17. Li Y, Tu JP, Huang XH, et al. Net-like SnS/carbon nanocomposite film anode materials for lithium ion batteries. *Electrochem Commum*. 2018;6:12185. doi:10.1016/j.elecom.2006.08.019
18. Yoon B-H, Koh Y-H, Park C-S, et al. Generation of large pore channels for bone tissue engineering using camphene-based freeze casting. *J Am Ceram Soc*. 2007;90(6):1774. doi:10.1111/j.1551-2916.2007.01670.x
19. Koo B-R, Oh S-T, Ahn H-J. Camphene effect for morphological change of electrospun SnO_2 nanofibres: from dense to fibre-in-hollow and to hollow nanostructures. *Mater Lett*. 2016;178:288. doi:10.1016/j.matlet.2016.05.016
20. Weiss IM, Muth C, Drumm R, et al. Thermal decomposition of the amino acids glycine, cysteine, aspartic acid, asparagine, glutamic acid, glutamine, arginine and histidine. *BMC Biophys*. 2018;11:2. doi:10.1186/s13628-018-0042-4
21. Zhao B, Zhuang H, Yang Y, et al. Composition-dependent lithium-storage performances of SnS/SnO_2 heterostructures sandwiching between spherical graphene. *Electrochim Acta*. 2019;300:253. doi:10.1016/j.electacta.2019.01.116
22. Ye H, Ki H, Jiang F, et al. In situ fabrication of nitrogen-doped carbon-coated SnO_2/SnS heterostructures with enhanced performance for lithium-storage. *Electrochim Acta*. 2018;266:170. doi:10.1016/j.electacta.2018.02.032
23. Shin D-Y, Lee JS, Ahn H-J. Hierarchical porous carbon nanofibers with ultrasmall-sized cobalt disulfide/tungsten disulfide hybrid composites for high-rate lithium-storage kinetics. *Appl Surf Sci*. 2021;550:149298. doi:10.1016/j.apsusc.2021.149298
24. Koo B-R, An H, Ahn H-J. High-surface area co-electrospun TiO_2 nanowires fabricated using shrinkage of polyvinylpyrrolidone for improved photovoltaic performance. *Ceram Int*. 2016;42:1666. doi:10.1016/j.ceramint.2015.09.120

25. Yoo G, Koo B-R, An G-H. Nano-sized split V_2O_5 with H_2O-intercalated interfaces as a stable cathode for zinc ion batteries without an aging process. *Chem Eng J*. 2022;434:134738. doi:10.1016/j.cej.2022.134738
26. Huang P-C, Shen Y-M, Brahma S, et al. SnS_x (x=1, 2) nanocrystals as effective catalysts for photoelectrochemical water splitting. *Catalysts*. 2017;7:252. doi:10.3390/catal7090252
27. Xiao Y, Su D, Wang X, et al. CuS microspheres with tunable interlayer space and micropore as a high-rate and long-life anode for sodium-ion batteries. *Adv Energy Mater*. 2018;8:1800930. doi:10.1002/aenm.201800930
28. Sung K-W, Shin D-Y, Ahn H-J. Boosting ultrafast Li storage kinetics of conductive Nb-doped TiO_2 functional layer coated on $LiMn_2O_4$. *J Alloys Compd*. 2021;870:159404. doi:10.1016/j.jallcom.2021.159404
29. Xu Q, Pu P, Zhao J, et al. Preparation of highly photoluminescent sulfur-doped carbon dots for Fe(III) detection. *J Mater Chem A*. 2015;3:542. doi:10.1039/c4ta05483k
30. Si W, Zhou J, Zhang S, et al. Tunable N-doped or dual N, S-doped activated hydrothermal carbonsderived from human hair and glucose for supercapacitor applications. *Electrochim Acta*. 2013;107:397. doi:10.1016/j.electacta.2013.06.065
31. Sung K-W, Koo B-R, Ah H-J. Hybrid nanocomposites of tunneled-mesoporous sulfur-doped carbon nanofibers embedded with zinc sulfide nanoparticles for ultrafast lithium-storage capability. *J Alloys Compd*. 2021;854:157206. doi:10.1016/j.jallcom.2020.157206
32. Choi M, William W, Hwang J, et al. A supercritical ethanol route for one-pot synthesis of tin sulfide–reduced graphene oxides and their anode performance for lithium ion batteries. *J Ind Eng Chem*. 2018;59:160. doi:10.1016/j.jiec.2017.10.020
33. Li W, Zhou M, Li H, et al. A high performance sulfur-doped disordered carbon anode for sodium ion batteries. *Energy Environ Sci*. 2015;8:2196. doi:10.1039/c5ee01985k
34. Shin D-Y, Jo H-G, Ahn H-J. Accelerating lithium-storage capability of cobalt sulfide encapsulated within anion dual-doped mesoporous carbon nanofibers. *Appl Surf Sci*. 2020;527:146895. doi:10.1016/j.apsusc.2020.146895
35. Shen X, Mu D, Shen S, et al. Enhanced electrochemical performance of ZnO-loaded/porous carbon composite as anode materials for lithium ion batteries. *ACS Appl Mater Interfaces*. 2013;5:3118. doi:10.1021/am400020n
36. Zhou Y, Wang Q, Zhu X, et al. Three-dimensional SnS decorated carbon nano-networks as anode materials for lithium and sodium ion batteries. *Nanomaterials*. 2018;8:135. doi:10.3390/nano8030135

SUPPORTING INFORMATION

Additional supporting information can be found online in the Supporting Information section at the end of this article.

How to cite this article: Sung K-W, Ahn H-J. Hierarchical carbon nanofibers@tin sulfide nanotube with sulfur-doped carbon layer for ultrafast lithium-storage capability. *Int J Energy Res*. 2022;46(13):18518-18528. doi:10.1002/er.8464